Research Square

Preprints are preliminary reports that have not undergone peer review.
They should not be considered conclusive, used to inform clinical practice,
or referenced by the media as validated information.

# Programmable Ultrasound Fields from a Single Laser Pulse

**Sayaka Ichihara**

sayaka.ichihara@ovgu.de

Otto-von-Guericke-Universität Magdeburg

**Pedro Quinto-Su**

Universidad Nacional Autónoma de México

**Claus-Dieter Ohl**

Otto-von-Guericke-Universität Magdeburg

**Article**

**Keywords:**

**Posted Date:** November 13th, 2026

**DOI:** https://doi.org/10.21203/rs.3.rs-11576702/v1

**License:** This work is licensed under a Creative Commons Attribution 4.0 International License.
Read Full License

**Additional Declarations:** No competing interests reported.

# Programmable Ultrasound Fields from a Single Laser Pulse

**Sayaka Ichihara*[1], Pedro A. Quinto Su[2], Claus-Dieter Ohl[1]**

[1]Faculty of Natural Sciences, Institute for Physics, Otto-von-Guericke-University Magdeburg, Universitätsplatz 2, 39106, Magdeburg, Germany

[2]Instituto de Ciencias Nucleares, Universidad Nacional Autónoma de Mexico, Apartado Postal 70-543, Coyoacán, Cd. Mx., 04510, Mexico

*Correspondence:sayaka.ichihara@ovgu.de

**Abstract**

Generating complex acoustic wavefronts with high spatial resolution and dynamic reconfigurability remains challenging. Existing approaches rely on phased-array transducers, static acoustic holograms, or time-delayed optical excitation, increasing complexity or limiting flexibility. Here, we demonstrate the synthesis of programmable broadband ultrasound fields by projecting a spatially structured nanosecond laser pulse onto a photoacoustic transducer. The optical intensity distribution defines the initial acoustic excitation, from which the desired wavefronts emerge through propagation. We experimentally demonstrate approximately planar wavefronts and single and multiple acoustic foci, finding quantitative agreement between measured and simulated pressure fields in both space and time, including diffraction-limited focusing. We identify the acoustic near field as the regime in which the desired wavefronts can be reconstructed. Our results establish single-shot photoacoustic holography as a method for generating broadband acoustic fields with predictable spatiotemporal evolution.

## 1. Introduction

Holographic techniques provide powerful means of generating complex acoustic fields. Acoustic wavefronts can be synthesized either using arrays of independently controlled ultrasound transducers, forming phased-array systems [1], or by encoding the phase or amplitude of an incident acoustic wave in the topography of a passive material, producing a static acoustic hologram [2].

Phased-array transducers offer dynamic control and allow acoustic fields to be reconfigured in real time for applications including acoustic levitation, particle manipulation and beam steering. However, they are often bulky and expensive, and their spatial resolution is limited by the finite number and spacing of the transducer elements. Three-dimensional printed acoustic holograms, in contrast, can achieve high spatial resolution

at low fabrication cost and require only a single driving transducer. Their principal limitation is that the encoded acoustic field is fixed after fabrication.

Despite this lack of reconfigurability, static acoustic holograms have enabled a broad range of applications. In biophotonics, for example, acoustic holograms have been used to guide light through strongly scattering tissue by creating localized pressure distributions that modify the refractive index and form acoustic waveguides [3]. Optimization-based holograms have also been designed to focus ultrasound while avoiding highly absorbing regions, thereby maximizing acoustic intensity at the target while reducing undesired heating [4].

More recently, planar binary-amplitude acoustic holograms have been fabricated by laser drilling arrays of subwavelength holes into thin metallic films [5]. Such holograms enable arbitrary shaping of acoustic fields, including letter-shaped intensity patterns, and can encode multiple acoustic images through frequency multiplexing.

The complementary strengths of phased arrays and static acoustic holograms have motivated approaches that combine high spatial resolution with dynamic reconfigurability. One example uses an acoustically transparent programmable metamaterial made from a cross-linked semicrystalline polymer. Local laser heating changes the speed of sound within selected regions, generating binary phase shifts of 0 and $\pi$. Because the phase pattern can be thermally written and erased, the acoustic hologram can be reconfigured repeatedly, although on timescales of several minutes.

A more direct strategy is to generate the acoustic field optically rather than modulating a pre-existing ultrasound wave. Structured laser illumination can excite spatially patterned photoacoustic sources and thereby produce complex acoustic fields without phased arrays or fabricated acoustic holograms. Previous implementations, however, have relied on temporal structuring, multiple optical excitations, or fixed optical elements. For example, Ref. [6] divided a microsecond laser pulse into a train of MHz photoacoustic pulses that were spatially shaped using a spatial light modulator to generate focused acoustic fields. Acoustic vortices have also been generated by passing collimated laser pulses through a transparent optical element with an azimuthally varying thickness before absorption [7]. In another approach, structured laser pulses with controlled temporal delays were used to focus laser-induced shock waves in thin liquid layers [8]. Generating a spatially programmable acoustic field from a single laser pulse, however, remains largely unexplored.

Here we demonstrate the generation of structured acoustic fields from a single nanosecond laser pulse. A spatial light modulator shapes the optical field incident on a carbon-nanotube–polydimethylsiloxane (CNT–PDMS) photoacoustic transducer, thereby encoding the spatial distribution of the acoustic source. We generate plane-wave-like fields as well as single and multiple acoustic foci and find quantitative agreement between their measured spatial and temporal evolution and numerical simulations. Our approach thus combines the spatial programmability of digital optics with single-shot

broadband photoacoustic generation.

## 2. Experiment

### 2.1. Principle of single-shot photoacoustic holography

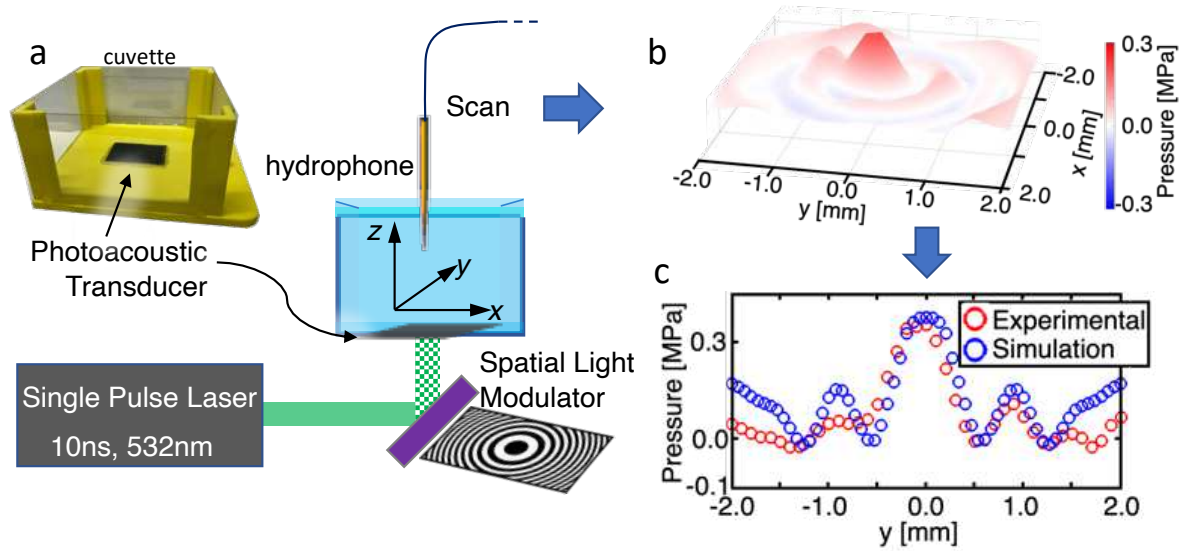



**Figure 1.** Principle of single-shot photoacoustic holography and its experimental realization. **a**, Schematic of the laser optical system incorporating a spatial light modulator (SLM) and experimental setup for measuring the acoustic field using a hydrophone. The spatial resolution of the SLM (HOLOEYE SLM) was 1920 $\times$ 1080 pixels with a pixel pitch of 8 µm. The cuvette was filled with distilled water. A photoacoustic transducer with a thickness of approximately 52 µm, was deposited on a 1 mm-thick glass substrate. The origin of the coordinate system was defined at the center of the reconstructed wave field generated by the SLM, corresponding to a rectangular laser beam encoding the digital phase hologram pattern (5.6 mm $\times$ 10.0 mm) after propagation and projection onto the photoacoustic transducer. **b**, Measured instantaneous acoustic field in the $x$-$y$ plane at $z$ = 5 mm, generated using a single-point hologram at $t$ = 3.31 µs. The laser energy was 402.3 $\pm$ 22.79 µJ. **c**, Pressure values along the $x$-axis in the pressure field in the $x$-$y$ plane. Red and blue plots represent the experimental measurements and numerical results, respectively.

Figure 1 illustrates the principle of single-shot photoacoustic holography and the corresponding experimental realization. A single nanosecond laser pulse is spatially modulated by a phase-only spatial light modulator (SLM). The structured optical intensity distribution defines the photoacoustic source distribution and is converted directly into the desired acoustic wavefront. In contrast to phased-array transducers or time-delayed optical excitation, the complete acoustic field is therefore synthesized from a single laser pulse.

The experimental setup is shown in Fig. 1a. A frequency-doubled Nd:YAG laser ($\lambda$ = 532 nm, $\tau_L$ = 10 ns) provided the optical excitation. The reconstructed optical field was projected onto a photoacoustic transducer consisting of a thin CNT–PDMS composite

layer deposited on a glass substrate. Carbon nanotubes efficiently absorb the laser pulse and convert the optical energy into heat, which is rapidly transferred to the surrounding PDMS. The resulting thermoelastic expansion generates a broadband acoustic pulse whose spatial distribution is determined by the optical illumination pattern.

To demonstrate the versatility of the method, we generated three classes of acoustic fields: plane-wave-like wavefronts, single acoustic foci, and multiple acoustic foci.

For the plane-wave-like acoustic field, we use a constant-amplitude pattern. In contrast, to enhance the acoustic field at specific confined locations, we calculate the holograms that for a single focus mimics a binary Fresnel lens: The binary holograms were calculated from the prescribed focal positions $F_i(x_i, y_i, z_i)$. The distance between a focal point and a point $(x, y, 0)$ on the photoacoustic transducer is

$$r_i = \sqrt{(x - x_i)^2 + (y - y_i)^2 + z_i^2}. \tag{1}$$

Assuming that the focal points are sufficiently far from the transducer and their spatial extent is negligible compared with the propagation distance, the complex acoustic field is approximated by

$$P(x, y) = \sum_{i=1}^{N} \exp(ik_0 r_i), \tag{2}$$

where $k_0$ denotes the acoustic wavenumber and $N$ is the number of prescribed focal points.The binary hologram is obtained from

$$\begin{cases} \mathrm{Re}(P(x, y)) \geq 0, & H(x, y) = 0, \\ \mathrm{Re}(P(x, y)) < 0, & H(x, y) = 1 \quad , \end{cases} \tag{3}$$

The phase on the SLM is this hologram $H(x, y)$ multiplied by a linear phase grating that separates the amplitude pattern from the zeroth diffraction order, which is blocked with an aperture in the Fourier plane. In this way the amplitude pattern $H(x, y)$ at the screen of the SLM is imaged with a lens onto the photoacoustic transducer (area approximately $5.6 \times 10.0$ mm$^2$) .

The generated acoustic field propagated through distilled water and was mapped with a needle hydrophone mounted on a motorized three-axis translation stage (Fig. 1a). Throughout this work, the arrival of the laser pulse on the photoacoustic transducer defines $t = 0$.

Figure 1b shows the instantaneous pressure field generated by a digital phase hologram designed to produce a single acoustic focus at $F(0, 0, 5.0)$ mm. The measured pressure field exhibits a pronounced central maximum surrounded by concentric diffraction rings

characteristic of an Airy-like pattern. The corresponding pressure profile along the $x$-axis agrees closely with the numerical simulation, as shown in Fig. 1c. In particular, the separation between the two innermost pressure minima is 1.2 mm experimentally and 1.1 mm in the simulation. Small discrepancies at larger radial distances are attributed to the Gaussian intensity profile of the experimental laser beam, whereas the numerical model assumes a spatially uniform photoacoustic source.

# 3. Results

## 3.1. Characterization of the photoacoustic pulse

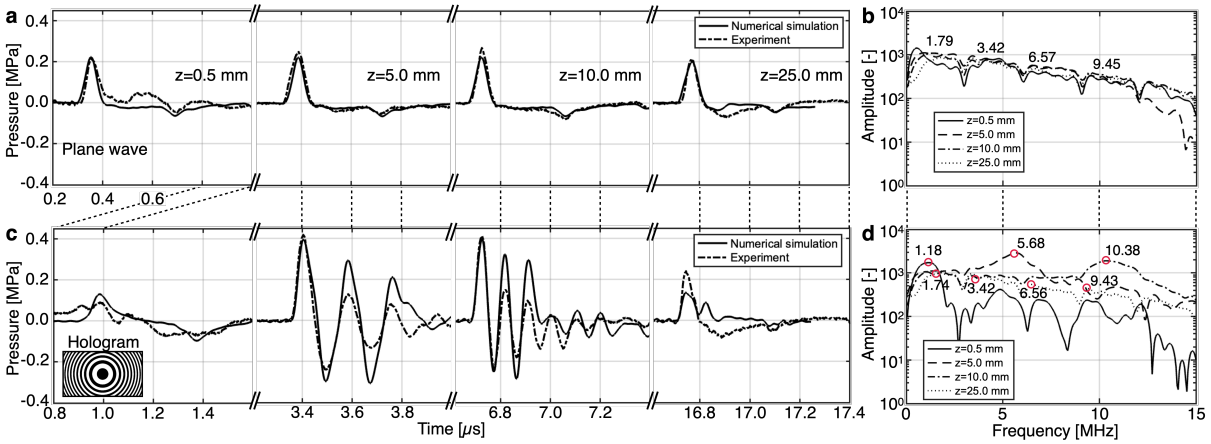



**Figure 2.** Temporal and spectral characteristics of the photoacoustic pulse. **a**, Pressure waveforms generated using a non-focusing phase hologram and measured at $z$ = 0.5 and 5.0 mm. Experimental measurements and numerical simulations are shown by the black and red curves, respectively. The laser pulse energy was $446.0 \pm 49.91$ µJ. **b**, Frequency spectrum of the pressure waveform measured at $z$ = 25.0 mm. Red circles indicate local maxima of the spectral amplitude. **c**, Axial evolution of the pressure waveform generated by a single-point phase hologram designed to focus at $F(0, 0, 5.0)$ mm. Pressure waveforms were measured at $(x, y) = (0, 0)$ for $z$ =0.5, 5.0, and 10.0 mm. Experimental measurements and numerical simulations are shown by the red and blue curves, respectively. The laser pulse energy was $447.1 \pm 41.91$ $\mu$J.

We first characterized the temporal and spectral response of the photoacoustic transducer with a plane-wave-like acoustic field, and a single-focus field (focus at $z$ = 5 mm). The first row in Fig. 2 has the data for the plane-wave-like field while the second row for the focused field. Figure 2a shows the pressure waveforms measured at $z$ = 0.5, 5, 10 and 25 mm (dotted lines), together with the corresponding numerical simulations (continuous lines). The amplitude and rise time of the initial positive pressure pulse remains nearly unchanged, while the following negative signal enhances with increasing propagation distance. This bipolar response originates from the mechanical constraint imposed by the glass substrate on the photoacoustic transducer [9, 10]. The simulations closely reproduce the measured waveforms at all propagation distances, including the arrival of the wavefront and the negative-pressure tail.

The characteristic acoustic transit time through the CNT–PDMS layer is $\tau_s = d_c/c_t \approx 50\,\text{ns}$ and thus exceeds the laser pulse duration, $\tau_L = 10\,\text{ns}$, satisfying the stress-confinement condition $\tau_L < \tau_s$ [11]. The measured pressure rise time is approximately 52 ns at all four propagation distances, in close agreement with the estimated acoustic transit time. The temporal width of the initial acoustic pulse is therefore governed primarily by the thickness of the photoacoustic transducer rather than by the duration of the laser pulse. Despite the 10 MHz measurement bandwidth, the observed 52 ns rise time remains consistent with the independently estimated $\sim$50 ns acoustic transit time, supporting a transducer thickness dominated response.

Figure 2b shows the corresponding frequency spectrum, obtained by Fourier transformation of the pressure waveform measured at $z$ =0.5, 5.0, 10.0, 25.0 mm. The analysis is restricted by the bandwidth of the hydrophone and amplifier that is 10 MHz. Within this range, the broadband photoacoustic pulse exhibits prominent spectral maxima at 1.79, 3.42, 6.57, and 9.45 MHz.

The pressure waveforms generated by the photoacoustic transducer using a single-point phase hologram are shown in Fig. 2c at axial distances of $z$ = 0.5, 5.0, 10.0, and 25.0 mm. The simulated waveforms agree closely with the experimental measurements at all propagation distances, reproducing the measured waveforms and wavefronts. Both the amplitude and waveform evolve during propagation owing to interference among the acoustic waves generated by the concentric ring sources. At the focus ($z$ = 5.0 mm), constructive interference produces a fourfold increase in acoustic pressure. With further propagation, the waveform progressively changes, and at $z$ = 25 mm it approaches the waveform observed for the plane-wave case shown in Fig. 2a.

The corresponding dominant frequencies are shown in Fig. 2d. For $z$ = 0.5, 5.0, and 10.0 mm, the dominant frequency increases from 1.18 to 5.68 and 10.68 MHz, respectively. The single-point phase hologram consists of three concentric rings, with mean radii of $\bar{R}_1$ = 1.2 mm, $\bar{R}_2$ = 2.0 mm, and $\bar{R}_3$ = 2.5 mm. This systematic increase is described by Eq. 6, which predicts an increase in the characteristic frequency of each ring with $z$ owing to the $z$-dependent arrival-time difference across its finite radial width. At $z$ = 25 mm, the waveform and dominant frequency approach those of the plane-wave case. This far-field evolution arises because the arrival-time separation between the innermost and outermost rings decreases with $z$; according to Eq. 9, it becomes comparable to the acoustic pulse duration ($\tau_r \sim 100$ ns) at the characteristic distance $z_r \approx 18.7$ mm. Thus, increasing $z$ progressively enhances the temporal overlap of contributions from the concentric rings, suppressing the distinct multi-cycle structure and yielding a waveform increasingly similar to that of a plane wave.

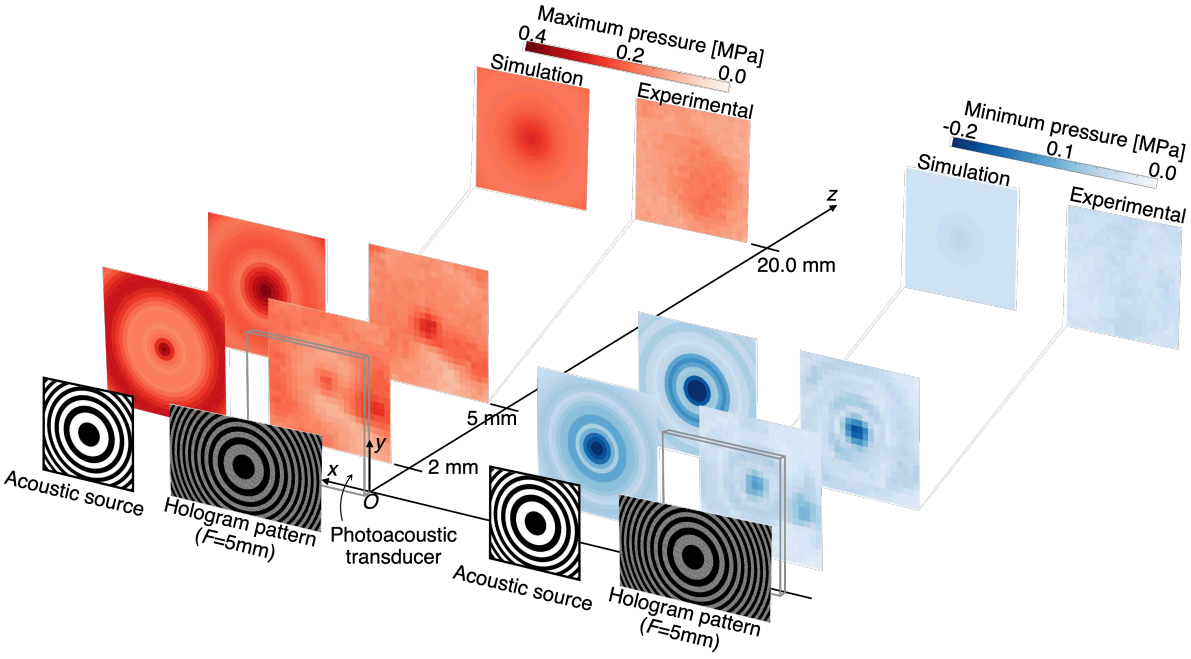



**Figure 3.** Spatial pressure distributions generated by a single-point phase hologram designed to focus at $(0, 0, 5.0)$ mm, showing maximum- and minimum-pressure distributions in the $x$–$y$ plane at $z$ = 2.0, 5.0, and 20.0 mm. Numerical simulations (left) are compared with hydrophone measurements (right). The laser pulse energies were $424.4 \pm 35.95$, $408.7 \pm 28.57$, and $402.3 \pm 22.79$ $\mu$J, respectively.

### 3.2. Spatial pressure distribution

We next characterize the spatial acoustic field generated by a single-point phase hologram designed to produce a focus at $(0, 0, 5.0)$ mm. Figure 3 shows the measured and simulated maximum- and minimum-pressure distributions in the $x$–$y$ plane at $z$ = 2.0, 5.0, and 20.0 mm. At $z$ = 2.0 and 5.0 mm, both experiment and simulation reveal a pronounced pressure maximum centred on the acoustic axis. At $z$ = 20.0 mm, the pressure distribution becomes substantially more uniform and no distinct central maximum is observed.

The minimum-pressure fields at $z$ = 2.0 and 5.0 mm additionally exhibit secondary and tertiary rings surrounding the central pressure extremum. These structures arise from diffraction by the Fresnel-like photoacoustic source distribution. The widths of the concentric rings in the projected source pattern are 0.57, 0.34, and 0.27 mm from the centre outwards. For comparison, the acoustic wavelength corresponding to the first spectral maximum at 1.74 MHz is approximately 0.86 mm. The comparable length scales of the acoustic wavelength and the source structure therefore give rise to pronounced diffraction.

The secondary rings are less clearly resolved in the measured maximum-pressure fields than in the simulations. This difference can be attributed in part to the lower spatial resolution of the measurements: the hydrophone was scanned in steps of 100 $\mu$m, com-

pared with a numerical grid spacing of approximately 17 $\mu$m. In addition, the simulations assume a spatially uniform source amplitude, whereas the experimental illumination has a non-uniform intensity profile.

### 3.3. Simultaneous generation of multiple acoustic foci

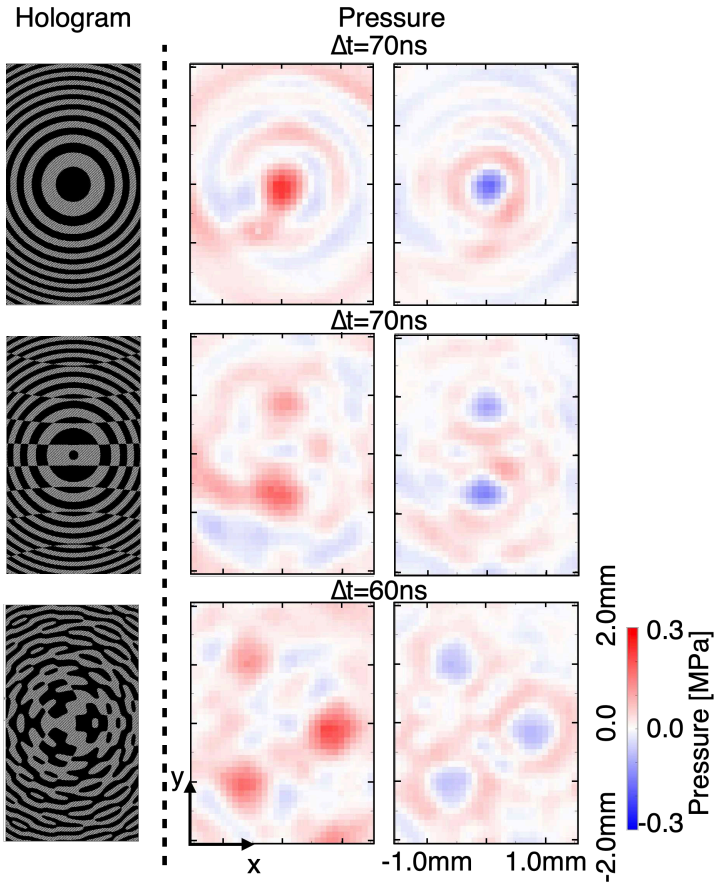



**Figure 4.** Single-shot generation of multiple acoustic foci. Instantaneous pressure fields generated by digital phase holograms designed to produce one (top), two (middle), or three (bottom) acoustic foci at $z$ = 5.0 mm. The corresponding phase holograms are shown on the left, and the measured pressure fields at two time points separated by $\Delta t$ = 60 or 70 ns are shown on the right. The prescribed transverse focal positions were $(0, 0)$ mm for the single-point hologram, $(0, \pm 0.7)$ mm for the two-point hologram, and $(0.8, 0)$ mm and $(-0.6, \pm 1.1)$ mm for the three-point hologram. The average laser pulse energies were $402.3 \pm 22.79$, $429.0 \pm 59.47$, and $477.2 \pm 46.77$ µJ, respectively.

We next demonstrate that single-shot photoacoustic holography can generate multiple acoustic foci simultaneously. Digital phase holograms were designed to produce one, two, or three prescribed focal points in the plane $z$ = 5.0 mm. Figure 4 shows the corresponding phase holograms and the measured instantaneous pressure fields at two time points separated by $\Delta t$ = 60 or 70 ns.

For the single-point hologram, designed to focus at $(0, 0, 5.0)$ mm, the two pressure

fields show the temporal evolution from a positive-pressure maximum to a subsequent negative-pressure maximum, with a time separation of $\Delta t \sim 60$–$70$ ns.

The same temporal evolution is observed for the two- and three-point holograms, but with the pressure field distributed among the prescribed focal positions. The positive- and negative-pressure maxima appear at the prescribed focal positions in the two instantaneous pressure fields, with a temporal separation of $\Delta t$ = 60 or 70 ns. For the single-point hologram, the pressure maximum is centred at $(x, y) = (0, 0)$; for the two-point hologram, the two maxima occur at $(x, y) = (\pm 0.7, 0)$ mm; and for the three-point hologram, they occur at $(x, y) = (0.8, 0)$ mm and $(-0.6, \pm 1.1)$ mm.

These measurements demonstrate that the spatial distribution of the acoustic field can be programmed independently of its temporal excitation. In particular, all prescribed foci are generated simultaneously from the same 10-ns laser pulse, without sequential excitation or time delays between the individual acoustic sources. The prescribed spatial structure of the acoustic field is therefore encoded in the digital phase hologram, while all foci are excited simultaneously by the same laser pulse.

### 3.4. Spatial resolution

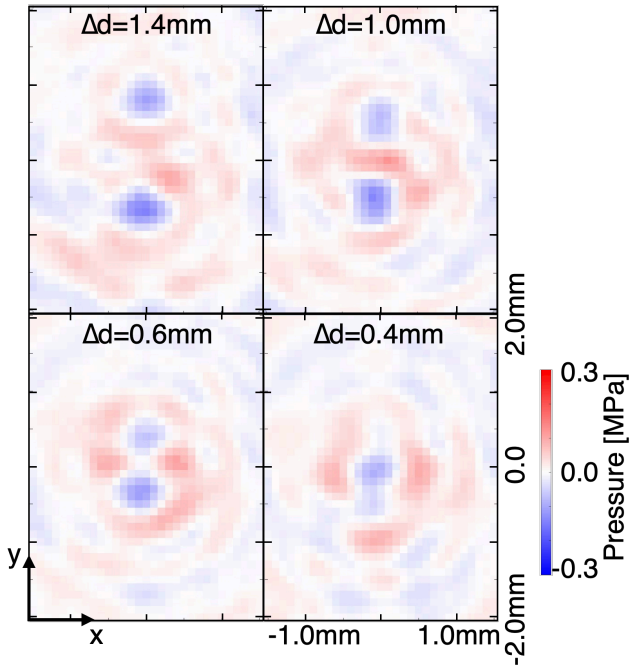



**Figure 5.** Spatial resolution of single-shot photoacoustic holography. Instantaneous pressure fields generated by two-point phase holograms with decreasing focal separation $d$, measured at $z$ = 5.0 mm and $t$ = 3.39 $\mu$s. From left to right, the prescribed separations are $\Delta d$ =1.4, 1.0, 0.6, and 0.4 mm. Two distinct pressure maxima remain resolved at $\Delta d$ = 0.6 mm and merge into a single maximum at $\Delta d$ = 0.4 mm.

Finally, we quantify the spatial resolution of the single-shot photoacoustic holography approach by systematically reducing the separation between two prescribed acoustic

foci. Figure 5 shows the instantaneous pressure fields generated by two-point phase holograms with focal separations $\Delta d$ ranging from 1.4 to 0.4 mm.

Two distinct pressure maxima are resolved for separations down to $\Delta d$ = 0.6 mm, whereas at $\Delta d$ = 0.4 mm the two maxima merge into a single pressure maximum. This resolution is consistent with the diffraction pattern of the single-point hologram. As shown in Fig. 1c, the single-focus pressure field has a central Airy-like disk with a diameter of approximately 1.2 mm. According to the Rayleigh criterion, two identical focal spots are just resolvable when their separation is approximately equal to the radius of the central Airy disk. The corresponding predicted resolution of approximately 0.6 mm agrees with the experimentally observed transition between resolved and unresolved acoustic foci.

The observed spatial resolution is therefore consistent with a limit set by acoustic diffraction rather than by the pixel resolution of the SLM. Under the present experimental conditions, independently prescribed acoustic foci can be resolved at separations of approximately 0.6 mm.

## 4. Conclusion

We have demonstrated single-shot photoacoustic holography for generating programmable acoustic fields from a single structured nanosecond laser pulse. A digital phase hologram displayed on an SLM shapes the optical excitation of a CNT–PDMS photoacoustic transducer, thereby encoding the spatial distribution of the acoustic source. The complete acoustic field is generated simultaneously from a single laser pulse, without phased-array transducers, fabricated acoustic holograms, or time-delayed optical excitation.

We experimentally demonstrated plane-wave-like fields as well as single and multiple acoustic foci and found close quantitative agreement with numerical simulations of their spatial and temporal evolution. The measurements further show that multiple prescribed foci are generated simultaneously and that their spatial resolution is consistent with the acoustic diffraction limit. These results establish single-shot photoacoustic holography as a route for converting structured light directly into complex broadband acoustic wavefronts. Because the complete acoustic field is encoded spatially and launched by a single laser pulse, the approach provides a means of generating reconfigurable acoustic fields on timescales ultimately limited by the optical modulation and laser repetition rate.

# 5. Method

## 5.1. Fabrication of photoacoustic transducer

Carbon nanotubes (CNTs; 0.05 g) were dispersed in toluene (99.8%; 0.5 g) by ultrasonication for 1 h. Polydimethylsiloxane (PDMS; SYLGARD 184) base (2.0 g) and curing agent (0.2 g) were mixed using a magnetic stirrer for 10 min and subsequently degassed under vacuum for 30 min. The CNT dispersion was added to the degassed PDMS mixture, followed by stirring for 10 min and a second vacuum-degassing step of 30 min.

The CNT–PDMS composite was deposited onto a 1-mm-thick glass substrate by spin coating. Three drops of the composite were dispensed onto the substrate and spin-coated at 300 rpm for 1 min. The coating procedure was repeated three times, followed by heating at 80 °C for at least 6 h to obtain the final CNT–PDMS photoacoustic transducer, as shown in Fig. 1(a).

## 5.2. Laser optical system

The optical configuration of the holographic projection system is shown in Figure. 6. A frequency-doubled Nd:YAG laser (Quantas Q2-SSQ2-E10-1064-SHG; $\lambda$ = 532 nm, pulse duration $\tau_L$ = 10 ns) was used for photoacoustic excitation. The pulse energy incident on the SLM was adjusted using a zero-order half-wave plate (WPH05M-532, Thorlabs) and a polarizing beamsplitter cube. It was then expanded using a pair of lenses with focal lengths of $-50$ and 150 mm and directed onto a phase-only spatial light modulator (SLM; PLUTO 2 VIS 096, HOLOEYE Photonics AG; $1920 \times 1080$ pixels, 8 $\mu$m pixel pitch).

The digital phase hologram $H$ displayed on the spatial light modulator (SLM) was generated from a binary pattern calculated using the prescribed focal positions $F_i$ and the screen size, as described by Eqs. (1)–(3). The modulated beam was then Fourier-transformed by a lens with a focal length of $f_1$=300 mm. An iris placed at the intermediate Fourier plane selected the first diffraction order while blocking the zeroth and higher diffraction orders. The selected first-order field was subsequently relayed to the photoacoustic transducer by a second lens with a focal length of $f_2$=200 mm, forming a two-lens 4-f imaging system with a transverse magnification of $|M| = f_2/f_1 = 2/3$. To compensate for the reduction in transverse size introduced by this imaging system, the calculated hologram pattern was scaled by a factor of $1/|M| = f_1/f_2 = 1.5$, thereby reproducing the prescribed focal positions and spatial dimensions at the transducer. The resulting optical field at the transducer had an approximate transverse size of $5.6 \times 10.0$ mm$^2$.

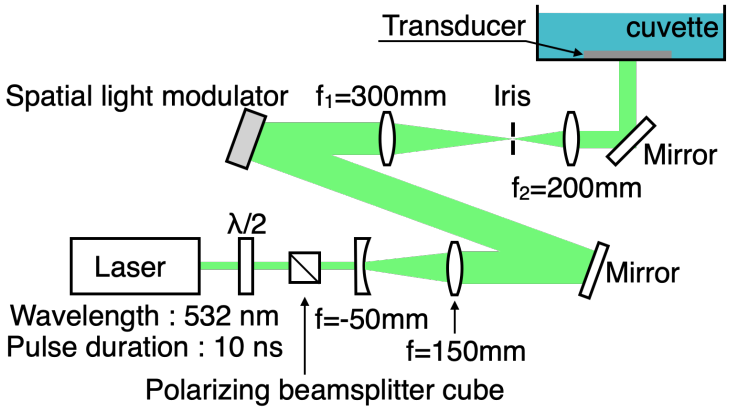



**Figure 6.** Schematic of the laser optical system incorporating a spatial light modulator (SLM).

### 5.3. Measurements

The optical absorbance of the CNT–PDMS layer deposited on the glass substrate was measured using a UV–Vis spectrophotometer (UV-2600, Shimadzu). At the excitation wavelength of 532 nm, the absorbance was 4.1, indicating strong optical absorption by the CNT–PDMS composite [12]. The thickness of the CNT–PDMS layer was measured by confocal microscopy (MarSurf CM explorer). The pulse energy of the first-order diffracted beam incident on the photoacoustic transducer was measured with an energy meter (ES120C, Thorlabs). For each measurement, 20 laser pulses were recorded to determine the mean pulse energy and its standard deviation.

The acoustic pressure field was measured using a needle hydrophone (Müller-Platte Needle Probe, Müller Instruments) mounted on a motorized three-axis translation stage (PI). The hydrophone signal was amplified using an MVA 10 voltage amplifier (Müller Instruments), resulting in a measurement bandwidth of 10 MHz. The hydrophone and laser were synchronized using a pulse generator (Model 525, Berkeley Nucleonics Corporation), with the laser pulse defining $t = 0$. At each measurement position, five pressure waveforms were recorded and averaged. Spatial pressure fields were obtained by scanning the hydrophone with a step size of 100 $\mu$m.

### 5.4. Numerical simulation

Numerical simulations were performed for the axisymmetric source patterns using the MATLAB k-Wave toolbox (v1.4.0) with the axisymmetric solver `kspaceFirstOrderAS`. Acoustic propagation was modeled by solving the first-order acoustic equations in a homogeneous, lossless fluid with a sound speed of $c_0 = 1489\ \mathrm{m\,s^{-1}}$ and a density of $\rho = 998\ \mathrm{kg\,m^{-3}}$.

The computational domain consisted of 168 $\times$ 1502 grid points in the radial and axial directions, respectively, with an isotropic grid spacing of $\Delta r = \Delta z = 16.6$ µm. The time step was 0.33 ns, corresponding to a Courant–Friedrichs–Lewy (CFL) number of 0.03.

Perfectly matched layers (PMLs) with a thickness of 20 grid points were applied at all boundaries to suppress artificial reflections.

The spatial distribution of the photoacoustic source was defined by the illuminated regions of the projected hologram pattern, with a uniform acoustic source amplitude assigned within these regions. The pressure waveform measured for the non-focusing hologram at $(r, z) = (0, 0.5\ \text{mm})$ was used as the temporal source function for all simulations. Thus, the experimentally measured temporal response of the photoacoustic transducer was retained, while the spatial source distribution was varied according to the respective projected optical intensity pattern. The simulations therefore model the propagation of the experimentally characterized photoacoustic pulse rather than the underlying thermoelastic generation process.

## 5.5. Acoustic waveform model

### 5.5.1 Characteristic frequency

A single-point hologram generates a concentric Fresnel-lens pattern, in which each annular region acts as an individual acoustic source. Because each ring has a finite radial width, pressure contributions originating from different radial positions within a ring travel different distances to the hydrophone and therefore arrive at different times. This arrival-time spread defines a characteristic temporal scale whose inverse increases with the propagation distance $z$.

We define the centre of the concentric-ring pattern as the origin and the acoustic propagation direction as the $z$-axis. The $m$-th ring extends from the inner radius $R_{2m-1}$ to the outer radius $R_{2m}$, such that $R_{2m-1} \leq R \leq R_{2m}$. The radial width and mean radius of the $m$-th ring are defined as $W_m = R_{2m} - R_{2m-1}$ and $\bar{R}_m = (R_{2m-1} + R_{2m})/2$, respectively.

For a hydrophone located on the $z$-axis, the propagation path from a radial position $R$ within the ring is $L(R, z) = \sqrt{R^2 + z^2}$. Thus, the propagation-path difference between the inner and outer boundaries of the $m$-th ring is

$$\Delta L_m(z) = \sqrt{R_{2m}^2 + z^2} - \sqrt{R_{2m-1}^2 + z^2}. \tag{4}$$

For $W_m \ll \sqrt{\bar{R}_m^2 + z^2}$, this path-length difference can be approximated as

$$\Delta L_m(z) \simeq W_m \frac{\bar{R}_m}{\sqrt{\bar{R}_m^2 + z^2}}. \tag{5}$$

The corresponding arrival-time difference is $\Delta t_m(z) = \Delta L_m(z)/c_0$. To quantify the characteristic temporal scale associated with the propagation delay across the $m$-th ring, we define the characteristic frequency scale $\nu_m(z)$ as the inverse of this arrival-time

difference:

$$\nu_m(z) = \frac{1}{\Delta t_m(z)} \simeq \frac{c_0}{W_m}\sqrt{1 + \frac{z^2}{\bar{R}_m^2}}. \tag{6}$$

This characteristic frequency scale increases with $z$ because the propagation-path difference, and hence the arrival-time difference, decreases as the observation point moves farther from the ring pattern. It characterizes the temporal scale associated with the intra-ring propagation delay rather than directly predicting the acoustic frequency spectrum.

### 5.5.2 Ring-wise arrival-time spread and characteristic frequency

To estimate the overall arrival-time spread across the ring pattern, we approximate each ring by its mean radius and consider the arrival-time difference between the innermost and outermost rings. The corresponding time separation is

$$\Delta t_{1,M}(z) = \frac{\sqrt{\bar{R}_M^2 + z^2} - \sqrt{\bar{R}_1^2 + z^2}}{c_0}. \tag{7}$$

In the far field, where $z \gg \bar{R}_M$, this expression reduces to

$$\Delta t_{1,M}(z) \simeq \frac{\bar{R}_M^2 - \bar{R}_1^2}{2c_0 z}. \tag{8}$$

We define a characteristic distance $z_r$ at which this arrival-time separation becomes comparable to the acoustic pulse duration $\tau_r$, such that $\Delta t_{1,M}(z_r) = \tau_r$. This yields

$$z_r \simeq \frac{\bar{R}_M^2 - \bar{R}_1^2}{2c_0\tau_r}. \tag{9}$$

At propagation distances comparable to or greater than $z_r$, the arrival-time separation between the innermost and outermost rings becomes comparable to or shorter than the pulse duration, promoting temporal overlap among contributions from different rings. Consistent with the experimentally observed waveform evolution, this overlap reduces the distinct multi-ring temporal structure, and the propagated waveform progressively approaches a more compact, plane-wave-like pulse shape.

## Acknowledgement

The authors gratefully acknowledge the financial support provided by OVGU for a research visit.

## Funding

This work was supported by the German Research Foundation (Deutsche Forschungsgemeinschaft, DFG) (Projects No. ME 1645/12-1 and No. OH 75/12-1). PAQS acknowledges funding from UNAM-PAPIIT (IN113424), CTIC-LANMAC, and SECIHTI (LN-299057 and CF-2023-I-657).


## Author Contributions

S.I. developed the methodology, performed the experiments and numerical simulations, collected and analyzed the data, and wrote the manuscript. P.A.Q.S. developed the methodology, performed the experiments, interpreted the results, and reviewed and edited the manuscript. C.-D.O. conceived and designed the study, supervised the work, and reviewed and edited the manuscript. P.A.Q.S. and C.-D.O. obtained the funding. All authors approved the final manuscript.

## Data Availability

Data sets generated during the current study are available from the corresponding author on reasonable request.

## References


[1] A. Marzo, S. A. Seah, B. W. Drinkwater, D. R. Sahoo, B. Long, and S. Subramanian, "Holographic acoustic elements for manipulation of levitated objects," *Nature communications*, vol. 6, no. 1, p. 8661, 2015.

[2] K. Melde, A. G. Mark, T. Qiu, and P. Fischer, "Holograms for acoustics," *Nature*, vol. 537, no. 7621, pp. 518–522, 2016.

[3] Q. Lin, Z. Li, B. Wang, M. Zhou, Y. Xie, D. Wang, C. Hou, R. Wang, X. Liu, X. Sun, *et al.*, "Acoustic hologram–induced virtual in vivo enhanced waveguide (ah-view)," *Science Advances*, vol. 10, no. 7, p. eadl2232, 2024.

[4] Y. Hertzberg and G. Navon, "Bypassing absorbing objects in focused ultrasound using computer generated holographic technique," *Medical physics*, vol. 38, no. 12, pp. 6407–6415, 2011.

[5] L.-S. Zeng, Z.-B. Lin, Z.-L. Li, Y. Yang, Y. Hu, Z. Chen, Y.-G. Peng, T. Ma, H.-R. Zheng, and X.-F. Zhu, "High-resolution manifold acoustic holography based

on high-pixel-array binary metasurfaces," *Advanced Materials*, vol. 37, no. 20, p. 2420229, 2025.

[6] A. Meyer, S. Gspan, , S. Bernet, and M. Ritsch-Marte, "Optoacoustic generation of a helicoidal ultrasonic beam," *Proceedings of SPIE*, vol. 4969, pp. 105–114, 2004.

[7] S. Gspan, A. Meyer, S. Bernet, and M. Ritsch-Marte, "Optoacoustic generation of a helicoidal ultrasonic beam," *Journal of the Acoustical Society of America*, vol. 115, no. 1, pp. 1142–1146, 2004.

[8] U. J. Gutiérrez-Hernández, F. De Colle, C.-D. Ohl, and P. A. Quinto-Su, "Transient time-delay focusing of shock waves in thin liquids," *Journal of Fluid Mechanics*, vol. 910, p. A27, 2021.

[9] R. Von Gutfeld and R. Melcher, "20-mhz acoustic waves from pulsed thermoelastic expansions of constrained surfaces," *Applied Physics Letters*, vol. 30, no. 6, pp. 257–259, 1977.

[10] E. Carome, N. Clark, and C. Moeller, "Generation of acoustic signals in liquids by ruby laser-induced thermal stress transients," *Applied Physics Letters*, vol. 4, no. 6, pp. 95–97, 1964.

[11] A. Doukas and T. J. Flotte, "Physical characteristics and biological effects of laser-induced stress waves," *Ultrasound in medicine & biology*, vol. 22, no. 2, pp. 151–164, 1996.

[12] J. Li, J. Xu, X. Liu, T. Zhang, S. Lei, L. Jiang, J. Ou-Yang, X. Yang, and B. Zhu, "A novel cnts array-pdms composite with anisotropic thermal conductivity for optoacoustic transducer applications," *Composites Part B: Engineering*, vol. 196, p. 108073, 2020.

## Supplementary Files

This is a list of supplementary files associated with this preprint. Click to download.

- Supplementary.pdf